

Universal Profiles of the Intracluster Medium from Suzaku X-Ray and Subaru Weak Lensing Observations *

N. OKABE,¹ K. UMETSU,² T. TAMURA,³ Y. FUJITA,⁴ M. TAKIZAWA,⁵ Y. -Y. ZHANG,⁶ K. MATSUSHITA,⁷ T. HAMANA,⁸ Y. FUKAZAWA,⁹ T. FUTAMASE,¹⁰ M. KAWAHARADA,³ S. MIYAZAKI,⁸ Y. MOCHIZUKI,⁷ K. NAKAZAWA,¹¹ T. OHASHI,¹² N. OTA,¹³ T. SASAKI,⁷ K. SATO,⁷ and S. I. TAM¹⁴

¹*Kavli Institute for the Physics and Mathematics of the Universe (WPI), Todai Institutes for Advanced Study, University of Tokyo, 5-1-5 Kashiwanoha, Kashiwa, Chiba 277-8583, Japan*

nobuhiro.okabe@ipmu.jp

²*Institute of Astronomy and Astrophysics, Academia Sinica, P.O. Box 23-141, Taipei 10617, Taiwan*

³*Institute of Space and Astronautical Science, Japan Aerospace Exploration Agency, 3-1-1 Yoshinodai, Chuo-ku, Sagami-hara, Kanagawa 229-8510, Japan*

⁴*Department of Earth and Space Science, Graduate School of Science, Osaka University, Toyonaka, Osaka 560-0043, Japan*

⁵*Department of Physics, Yamagata University, Kojirakawa-machi 1-4-12, Yamagata 990-8560, Japan*

⁶*Argelander-Institut für Astronomie, Universität Bonn, Auf dem Hügel 71, 53121 Bonn, Germany*

⁷*Department of Physics, Tokyo University of Science, 1-3 Kagurazaka, Shinjyuku-ku, Tokyo 162-8601, Japan*

⁸*National Astronomical Observatory of Japan, Mitaka, Tokyo 181-8588, Japan*

⁹*Department of Physical Science, Hiroshima University, 1-3-1 Kagamiyama, Higashi-Hiroshima, Hiroshima 739-8526, Japan*

¹⁰*Astronomical Institute, Tohoku University, Aramaki, Aoba-ku, Sendai 980-8578, Japan*

¹¹*Department of Physics, The University of Tokyo, 7-3-1 Hongo, Bunkyo-ku, Tokyo 113-0033, Japan*

¹²*Department of Physics, Tokyo Metropolitan University, 1-1 Minami-Osawa, Hachioji, Tokyo 192-0397, Japan*

¹³*Department of Physics, Nara Women's University, Kitauoyanishi-machi, Nara, Nara 630-8506, Japan*

¹⁴*Department of Physics, National Taiwan University, Taipei 10617, Taiwan*

(Received ; accepted)

Abstract

We conduct a joint X-ray and weak-lensing study of four relaxed galaxy clusters (Hydra A, A478, A1689 and A1835) observed by both *Suzaku* and Subaru out to virial radii, with an aim to understand recently-discovered unexpected feature of the intracluster medium (ICM) in cluster outskirts. We show that the average hydrostatic-to-lensing total mass ratio for the four clusters decreases from $\sim 70\%$ to $\sim 40\%$ as the overdensity contrast decreases from 500 to the virial value. The average gas mass fraction from lensing total mass estimates increases with cluster radius and agrees with the cosmic mean baryon fraction within the virial radius, whereas the X-ray-based gas fraction considerably exceeds the cosmic values due to underestimation of the hydrostatic mass. We also develop a new advanced method for determining normalized cluster radial profiles for multiple X-ray observables by simultaneously taking into account both their radial dependence and multivariate scaling relations with weak-lensing masses. Although the four clusters span a range of halo mass, concentration, X-ray luminosity and redshift, we find that the gas entropy, pressure, temperature and density profiles are all remarkably self-similar when scaled with the weak-lensing M_{200} mass and r_{200} radius. The entropy monotonically increases out to $\sim 0.5r_{200} \sim r_{1000}$ following the accretion shock heating model $K(r) \propto r^{1.1}$, and flattens at $\gtrsim 0.5r_{200}$. The universality of the scaled entropy profiles indicates that the thermalization mechanism over the entire cluster region ($> 0.1r_{200}$) is controlled by gravitation in a common way for all clusters, although the heating efficiency in the outskirts needs to be modified from the standard $r^{1.1}$ law. The bivariate scaling functions of the gas density and temperature reveal that the flattening of the outskirts entropy profile is caused by the steepening of the temperature, rather than the flattening of the gas density.

Key words: galaxies: clusters: individual (Hydra A ; A478 ; A1689 ; A1835) - gravitational lensing: weak - X-rays: galaxies: clusters

1. Introduction

Recent studies with the *Suzaku* X-ray satellite (Mitsuda et al. 2007) have reported detections of very faint X-ray

emission in the outskirts of galaxy clusters thanks to its low and stable particle background. These *Suzaku* observations revealed unexpected observational features of the intracluster medium (ICM) in the cluster outskirts (e.g. Fujita et al. 2008; Bautz et al. 2009; Kawaharada et al. 2010; Hoshino et al. 2010; Simionescu et al. 2011; Sato et al. 2012; Walker et al. 2012b,a, 2013; Ichikawa et al.

* Based on data collected at Subaru Telescope, which is operated by the National Astronomical Observatory of Japan.

2013; Reiprich et al. 2013): The observed gas temperature sharply declines beyond about half the cluster virial radius. In the cluster outskirts, the gas temperature is at most 20-50% of those at intermediate radii (from one-fourth to half the virial radius). The gas entropy profile $K(r) = k_B T(r)/n_e^{2/3}(r)$ flattens beyond about half the virial radius, in contrast to predictions of accretion shock-heating models (e.g. Tozzi & Norman 2001; Ponman et al. 2003). If all kinetic energy of the infalling gas is instantly thermalized by the accretion shock, the entropy profile is predicted to increase with cluster radius as $K(r) \propto r^{1.1}$ (Tozzi & Norman 2001), as supported by *Chandra* and *XMM-Newton* observations of cluster central regions (e.g. Cavagnolo et al. 2009; Pratt et al. 2010). In fact, the entropy in the interior region is enhanced compared to the $r^{1.1}$, as also shown in Walker et al. (2013). The outskirts entropy from *Suzaku* is systematically lower than these model predictions as well as those extrapolated from observations in the central regions. These pieces of evidence indicate that the majority of electrons in the cluster outskirts are not yet thermalized, so that the thermal pressure in the outskirts is not sufficient to fully balance with the total gravity of the cluster. Furthermore, Kawaharada et al. (2010) and Ichikawa et al. (2013) showed that the anisotropic distributions of gas temperature and entropy in the outskirts are correlated with large-scale structure of galaxies outside the central clusters. Sato et al. (2012) found that the gas density distribution is correlated with large-scale structure of galaxies. These spatial correlations between thermodynamic properties of the ICM and large-scale environments indicate that the physical processes in the cluster outskirts are influenced by surrounding cosmological environments.

Several interpretations have been proposed to explain the presence of low entropy gas in the ICM. For example, hot ions could provide main thermal-pressure support (Hoshino et al. 2010) if the electron in the outskirts are not yet fully thermalized. This could be possible because the timescale of thermal equilibrium of the electrons by Coulomb collisions is much longer than that of the ions. However, this scenario ignores the fact that the timescale for electrons to achieve thermal equilibrium governed by wave-particle interactions of plasma kinetic instabilities is much shorter than that by Coulomb collisions. Alternatively, the kinetic energy of bulk and/or turbulent motions could contribute to some fraction of the total pressure to fully balance with the gravity (Kawaharada et al. 2010). Lapi et al. (2010) and Cavaliere et al. (2011) proposed that the outer slope of the potential becomes shallower due to the acceleration of cosmic expansion and hence the efficiency of accretion shock heating is weakened. Fujita et al. (2013) proposed that the accretion of cosmic-rays at cluster formation shocks consumes kinetic energy of infalling gas and decreases the entropy of the downstream gas. A high degree of gas clumpiness in cluster outskirts could lead to an overestimate of the observed gas density, causing the apparent flattening of the derived entropy profile (Nagai & Lau 2011).

Simionescu et al. (2011) found that the gas mass fraction in the Perseus cluster based on hydrostatic mass estimation exceeds the cosmic baryon fraction within the virial radius, and attributed this apparent excess to gas clumpiness. However, their X-ray-only analysis suffers from the inherent assumption of hydrostatic equilibrium. In particular, in light of the observed low gas temperature and entropy in cluster outskirts, the ICM there is expected to be out of hydrostatic equilibrium. Therefore, accurate and direct cluster mass determinations without the hydrostatic equilibrium assumption are essential for understanding the physical state of the ICM in cluster outskirts.

Weak gravitational lensing techniques are complementary to X-ray observations because weak-lensing mass estimates do not require any assumptions on cluster dynamical states. A coherent distortion pattern of background galaxy shapes caused by the gravitational potential of clusters enables us to recover the cluster mass distribution (e.g., Bartelmann & Schneider 2001). A comparison of X-ray and weak-lensing cluster mass estimates provides a stringent test of the level of hydrostatic equilibrium (e.g., Zhang et al. 2010; Kawaharada et al. 2010; Mahdavi et al. 2013), which is important for empirically understanding the systematic bias in cluster mass estimates and for constructing well-calibrated cluster mass-observable relations for cluster cosmology (e.g. Vikhlinin et al. 2009b). In particular, multi-wavelength cluster datasets of high quality covering the entire cluster region are crucial for a diagnostic of the ICM states out to the virial radius.

In the present paper we compile a sample of four massive clusters (Hydra A, A478, A1689, A1835) which have been deeply observed out to the virial radius with the *Suzaku* X-ray satellite and the Subaru Telescope, and perform a joint X-ray and weak-lensing analysis to study the relations between the total mass and ICM in this cluster sample. The four clusters have different properties of the X-ray luminosity (L_X), average temperature ($\langle k_B T \rangle$) and redshift (z), as summarized in Table 1. The X-ray luminosities differ by one order of magnitude and the redshifts are at $0.05 \lesssim z \lesssim 0.25$. The typical integration time with *Suzaku* to detect faint X-ray emission from cluster outskirts is much longer than that for cluster central regions and multi-pointing Subaru observations are required to cover the entire region of nearby *Suzaku* targets. Therefore our current sample is limited only to four objects. Weak-lensing and X-ray analyses are briefly described in Section 2. In Section 3, we compare our weak-lensing mass measurements with X-ray properties of the ICM as function of the cluster overdensity radius. The results are summarized in Section 4. In the paper, we use $\Omega_{m,0} = 0.27$, $\Omega_\Lambda = 0.73$ and $H_0 = 70 h_{70} \text{ kms}^{-1} \text{ Mpc}^{-1}$.

2. Data Analysis

2.1. Subaru lensing Analysis

We carried out weak-lensing analyses of individual clusters in our sample using wide-field multi-band observations taken with the Suprime-Cam (Miyazaki et al. 2002) at the prime focus of the 8.2-m Subaru Telescope.

We securely selected background source galaxies in order to avoid contamination by unlensed cluster galaxies. We measure the mass M_Δ at overdensities of $\Delta = 2500, 1000, 500, 200$ and the virial overdensity $\Delta_{\text{vir}} \sim 100 - 110$ (Nakamura & Suto 1997). Here, M_Δ represents the mass enclosed within a sphere of radius r_Δ inside which the mean interior density is Δ times the critical mass density, $\rho_{\text{cr}}(z)$, at the redshift, z .

For A1689 ($z = 0.1832$), we employ the nonparametrically-deprojected spherical mass model from a joint strong-lensing, weak-lensing shear and magnification analysis described in Kawaharada et al. (2010) and Umetsu & Broadhurst (2008). We fit the tangential (reduced) shear profile for the other three clusters with a parametrized mass model. Here, the tangential distortion signal, the mean ellipticity of background galaxies tangential to the cluster center, is obtained as a function of projected distance from the brightest cluster galaxy (BCG).

Our weak-lensing analysis with new Subaru observations of Hydra A ($z = 0.0538$) and A478 ($z = 0.0881$) is described in details in Okabe et al. (2014). As for A1835 ($z = 0.25280$), we have reanalyzed the Subaru data using new background selection of Okabe et al. (2013), and measured the mass profile in combination with strong lensing data (Richard et al. 2010). We employ the universal mass profile of Navarro et al. (hereafter NFW; 1996, 1997) which is empirically motivated by numerical simulations of collisionless cold dark matter. The NFW density profile is given by the following form:

$$\rho_{\text{NFW}}(r) = \frac{\rho_s}{(r/r_s)(1+r/r_s)^2}, \quad (1)$$

where ρ_s is the central density parameter and r_s is the scale radius. The halo concentration is defined by $c_\Delta = r_\Delta/r_s$. The resulting M_{200} is listed in Table 1.

Since the uncertainty of mass estimates by joint strong- and weak-lensing measurements is much smaller than those by weak-lensing-only measurements, we shall apply unweighted averaging in our cluster ensemble analysis.

2.2. *Suzaku* X-ray Analysis

The *Suzaku* studies for Hydra A, A478, A1689 and A1835 are described in details in Sato et al. (2012), Mochizuki et al. (2014), Kawaharada et al. (2010) and Ichikawa et al. (2013), respectively. We here briefly summarize the analyses. Low and stable particle background of *Suzaku* is powerful to detect diffuse faint X-ray emission beyond about half of the virial radius. On the other hand, high angular resolutions of *Chandra* and *XMM-Newton* have advantages to measure the ICM properties within about half of the virial radius. A joint X-ray study, combined with these datasets in different sensitivities and resolutions, well constrains the temperature and density profiles from the cores out to virial radii (Sato et al. 2012; Ichikawa et al. 2013; Mochizuki et al. 2014). We also found that the X-ray observables (the density, temperature, pressure and entropy) derived by *Suzaku*, *XMM-Newton* and *Chandra* agree with each other at overlapping

radii (Zhang et al. 2007; David et al. 2001; Sanderson et al. 2005). The X-ray surface brightness profile of *Suzaku* is consistent with the *ROAST* flux. The thermal pressure out to virial radius measured by *Suzaku* is also in good agreement with the *Planck* flux of the Sunyaev-Zel'dovich (SZ) effect on the cosmic microwave background (CMB) (Ichikawa et al. 2013; Mochizuki et al. 2014). We assume the spherical distribution to derive hydrostatic equilibrium masses and gas masses from best-fit functions of the temperature and gas density profiles, as described in our earlier papers (Kawaharada et al. 2010; Sato et al. 2012; Ichikawa et al. 2013; Mochizuki et al. 2014). In the cluster outskirts, we use azimuthal averages of *Suzaku* X-ray observables for A478, A1689 and A1835. As for Hydra A, we use unweighted averages of observables in two directions of an over-dense filamentary structure of galaxies and a low density void environment outside the cluster. In the central regions, X-ray observables measured by the *XMM-Newton* or *Chandra* are added to the *Suzaku* data. The references are listed in Table 1. We take into account only statistical errors.

3. Comparison of Lensing and X-ray measurements

3.1. Comparison of Hydrostatic Equilibrium Mass and Weak-lensing Mass

Weak-lensing mass measurements do not require the hydrostatic equilibrium assumption, and are complementary to X-ray measurements. It is of critical importance to compare these two independent mass estimates for understanding the physical state of the ICM as well as for examining the degree of hydrostatic equilibrium (Kawaharada et al. 2010; Sato et al. 2012; Ichikawa et al. 2013; Mochizuki et al. 2014). Our unique dataset of wide-field *Suzaku* and Subaru observations enables us to directly compare X-ray and lensing masses from the cluster core to the virial radius.

Figure 1 shows the hydrostatic-to-lensing total mass ratio as a function of overdensity Δ with $\Delta = 2500, 1000, 500, 200$ and Δ_{vir} . To avoid aperture-induced errors in enclosed-mass measurements, we calculate the X-ray mass inside the same radius determined by lensing analysis. Overall, the mass-ratio profiles decrease outward in a similar manner. We show in the figure that the unweighted average of the mass ratios (large black circles) monotonically decreases as the overdensity Δ decreases. We fit the average profile with the functional form of $\ln(\langle M_{\text{H.E.}}/M_{\text{WL}} \rangle) = A + B \ln(\Delta)$. The best-fit slope is $B = 0.22 \pm 0.07$. The overdensity dependence is thus detected at the 3σ level. The mass discrepancy is negligible at a high overdensity of $\Delta = 2500$. However, we find that the X-ray hydrostatic mass can only account for $\sim 70\%$ and $\sim 40\%$ of the lensing mass at $\Delta = 500$ and Δ_{vir} , respectively.

Similar results were found inside r_{500} by previous observational studies and numerical simulations. Mahdavi et al. (2013) compared their weak-lensing masses with X-ray masses for 50 clusters, finding that the X-ray to weak-

Table 1. Target Properties. The X-ray luminosity is retrieved from the MCXC catalog (Piffaretti et al. 2011). The fourth and fifth column are the average X-ray temperature and weak-lensing masses, respectively. The references of the *Suzaku*, *Chandra* and *XMM-Newton* data are listed.

Name	z	L_X [10^{45}ergs^{-1}]	$\langle k_B T \rangle$ [keV]	M_{200} [$h_{70}^{-1} 10^{14} M_\odot$]	<i>Suzaku</i>	<i>XMM-Newton/Chandra</i>
Hydra A	0.0538	0.27	3.0	$3.72^{+2.11}_{-1.44}$	Sato et al. (2012)	David et al. (2001)
A 478	0.0881	0.72	7.0	$13.05^{+4.12}_{-3.30}$	Mochizuki et al. (2014)	Sanderson et al. (2005)
A 1689	0.1832	1.25	9.3	$16.73^{+4.88}_{-3.44}$	Kawaharada et al. (2010)	Zhang et al. (2007)
A 1835	0.2528	1.97	8.0	$10.35^{+2.80}_{-2.40}$	Ichikawa et al. (2013)	Zhang et al. (2007)

lensing total mass ratio for their full sample is 0.92 ± 0.05 at $\Delta = 2500$, 0.89 ± 0.05 at $\Delta = 1000$, and 0.88 ± 0.05 at $\Delta = 500$, respectively, Hydrodynamical numerical simulations (Nagai et al. 2007b; Piffaretti & Valdarnini 2008; Lau et al. 2009, 2013; Nelson et al. 2014) found that the hydrostatic-to-true total mass ratio within r_{500} is more or less comparable with our results. On the other hand, the hydrostatic-to-true mass ratio within r_{200} is found to be $\sim 80 - 90\%$, which is much larger than our results. Hence, there is a substantial discrepancy between our results and numerical simulations in the cluster outskirts at low overdensities $\Delta \lesssim 200$. Such a large bias can be caused if the hydrostatic cumulative mass unphysically decreases with radius at cluster outskirts (e.g. Kawaharada et al. 2010; Sato et al. 2012). We will discuss the possible deviations of X-ray observables in Section 3.6.

Measuring and quantifying any bias in hydrostatic mass estimates is one of the key issues for cluster cosmology. Lensing observations suffer from noisy projection effects, but can provide unbiased cluster mass estimates in a statistical sense if one can avoid an orientating bias (e.g., Meneghetti et al. 2014). In particular, stacked cluster lensing measurements (Okabe et al. 2010a, 2013; Oguri et al. 2012; Umetsu et al. 2011, 2014), which are insensitive to systematics due to projection effects, allow us to determine the representative mass profile for a cluster sample.

Our cluster sample is small but solely defined by the current availability of both *Suzaku* and Subaru observations. We note that, although A1689 is a well-known strong-lensing cluster, the overall trends in the observed mass ratios are common to all clusters. Our results suggest that the degree of breakdown of the hydrostatic equilibrium assumption can vary substantially with cluster radius, indicating that an accurate characterization of the radial-dependent mass bias is crucial for cluster cosmology. This has direct consequences for the origin and degree of the apparent *tension* between the number counts of SZ clusters detected by *Planck* compared to those predicted by the *Planck* CMB cosmology (Planck Collaboration et al. 2013b). In their cluster cosmology analysis, Planck Collaboration et al. (2013b) adopted *XMM-Newton*-based hydrostatic mass estimates and calibrated their cluster masses M_{500} assuming a constant bias of 20%. Their assumed bias is smaller than but compatible with our re-

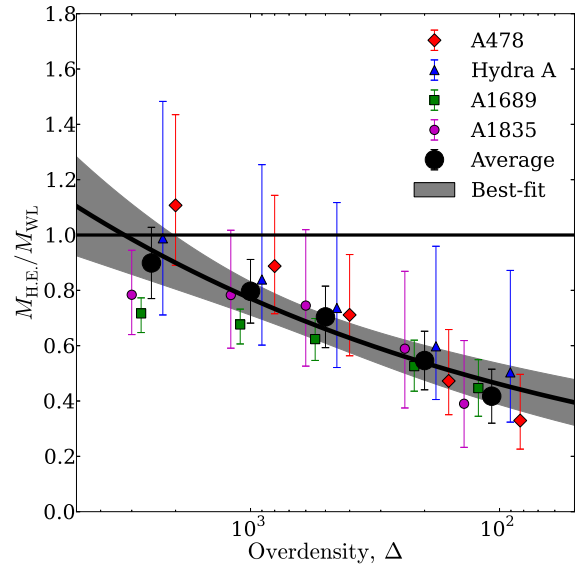


Fig. 1. X-ray hydrostatic to weak-lensing total mass ratios as a function of the density contrast Δ . Red diamonds, blue triangle, green squares, magenta circles and large black circles denote the mass ratios for A478, Hydra A, A1689, A1835 and the unweighted average of the 4 clusters, respectively. From left to right, the data points with error bars represent the mass ratios at $\Delta = 2500, 1000, 500, 200$ and Δ_{vir} , respectively. The mass ratios for the clusters are horizontally offset for visual clarity. The black-solid curve and gray-solid area are the best-fit profile and 1σ uncertainty.

sults.¹ Note that, since the size of our sample is small, it is essential to conduct further systematic studies with larger samples of X-ray and weak-lensing data covering the entire cluster region.

3.2. Gas Fraction

We have computed the gas mass fractions for the four clusters, $f_{\text{gas}}(< r) = M_{\text{gas}}(< r) / M_{\text{WL}}(< r)$, as a function of the density contrast Δ (Figure 2). Here, the gas mass $M_{\text{gas}}(< r)$ is measured inside the aperture radius r_Δ determined by weak-lensing analysis. Compared to the total mass ratio, intrinsic scatter in gas fraction for individual

¹ Again, the X-ray mass has been measured within the weak-lensing determined aperture radius in our study.

clusters is large.

Using the lensing total mass estimates, we find that the gas fractions within the virial radius are lower than or comparable to the cosmic mean baryon fraction (Hinshaw et al. 2013; Planck Collaboration et al. 2013a), finding no evidence for the excess gas fraction relative to the cosmic value.

An apparent baryon excess within r_{200} was reported in the Perseus cluster on the basis of *Suzaku* hydrostatic mass estimates (Simionescu et al. 2011). However, as discussed in Section 3.1, since the X-ray hydrostatic masses are underestimated especially at large cluster radii, the X-ray-based gas fractions can be largely overestimated and exceed the cosmic mean baryon fraction (e.g., Sato et al. 2012; Ichikawa et al. 2013; Mochizuki et al. 2014). Weak-lensing mass determinations are needed to avoid such systematics.

Figure 2 shows that the unweighted average of the gas fractions increases as the overdensity decreases. We fit the average gas fraction profile with the functional form of $\langle f_{\text{gas}} \rangle = A + B \ln(\Delta)$. The best-fit normalization and slope are $A = 0.250 \pm 0.065$ and $B = -0.018 \pm 0.009$, respectively. The average gas fraction within the virial radius agrees within errors with the cosmic mean baryon fractions from the *WMAP* (Hinshaw et al. 2013) and *Planck* (Planck Collaboration et al. 2013a) experiments.

3.3. Outskirts Entropy

The gas entropy profiles for relaxed clusters are observed to be fairly universal over a wide radial range (Walker et al. 2012a; Sato et al. 2012), increasing following a power-law ($\propto r^{1.1}$) out to intermediate radii and then flattening off from $\sim 0.5r_{\text{vir}}$ to r_{vir} . Accordingly, the observed entropy in the outskirts is significantly lower than that extrapolated with the power-law form of $K(r) \propto r^{1.1}$. The scaled entropy profiles from *Suzaku* observations are well fitted by a universal function in which the entropy flattening and turnover are characterized by the virial radius or r_{200} (Walker et al. 2012a; Sato et al. 2012), suggesting that there is a physical correlation between the outskirts entropy and the virial mass.

Here we investigate a correlation between the outskirts entropy and the virial mass by using our lensing-derived virial mass estimates. We adopt the average entropy $K(r) = k_B T / n_e^{2/3}$ in the radial range $r_{500} - r_{\text{vir}}$ as the outskirts entropy, K_{out} . Since the observed entropy profiles in the outskirts are fairly flat, the results here are insensitive to the choice of the radial range. We fit the functional form $\ln(K_{\text{out}}) = A + B \ln(M_{\text{vir}} E(z))$ for our sample of four clusters, where $E(z) = (\Omega_{m,0}(1+z)^3 + \Omega_\Lambda)^{1/2}$ is the dimensionless Hubble expansion rate, A is the normalization and B is the slope. The best-fit normalization and slope are $A = 5.40 \pm 0.57$ and $B = 0.69 \pm 0.25$, respectively. We find a tight correlation between K_{out} and $E(z)M_{\text{vir}}$ as shown in left panel of Figure 3. Similarly, we also compare the relationship between the outskirts entropy and M_{200} , finding again a tight correlation ($A = 5.57 \pm 0.50$ and $B = 0.69 \pm 0.24$). Our results suggest that the gravity of the cluster has an important effect on the thermaliza-

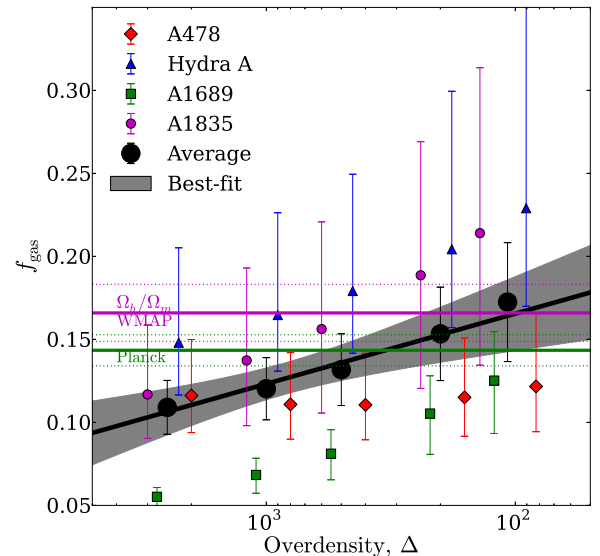


Fig. 2. Gas mass fraction, $M_{\text{gas}}/M_{\text{WL}}$, from weak-lensing total mass estimates, shown as a function of the density contrast Δ . Red diamonds, blue triangle, green squares, magenta circles and large black circles denote the mass ratios for A478, Hydra A, A1689, A1835 and the unweighted average of the 4 clusters, respectively. The data points for the 4 clusters at each density are horizontally offset for visual clarity. The horizontal-solid lines with dotted error bars are the cosmic mean baryon fractions from *WMAP* (Hinshaw et al. 2013) and *Planck* (Planck Collaboration et al. 2013a) with their respective 1σ uncertainties. The black-solid curve and gray-solid area show the best-fit profile and the 1σ uncertainty interval.

tion process even in the outskirts. However, since the outskirts entropy is lower than predicted by the accretion shock heating model (Tozzi & Norman 2001), the shock heating is not sufficient to explain the observations.

A possible mechanism for weakening of accretion shock heating in cluster outskirts has been proposed by Lapi et al. (2010) and Cavaliere et al. (2011). According to their scenarios, the outer slope of the gravitational potential becomes progressively shallower in the accelerating universe, and the background gas density is decreased at late times accordingly. Then the entropy production is reduced by the slowdown in the growth of outskirts. Their model predicts that the outskirts entropy is anti-correlated with the halo concentration at a fixed mass because the concentration is related to the formation epoch. The two clusters A478 and A1689 have similar virial masses, albeit different concentration parameters: $c_{\text{vir}} \sim 4$ for the former (Okabe et al. 2014) and $c_{\text{vir}} \sim 13$ for the latter (Umetsu & Broadhurst 2008). We do not find any significant difference in the outskirts entropy between the two clusters. However, since the concentration parameter is sensitive to halo triaxiality and orientation (e.g. Oguri & Keeton 2004) and the cluster redshifts are different, the uncertainty from such other factors is large. Therefore, a further systematic study with a large statistical sample is

required to investigate this possible correlation.

Nagai & Lau (2011) proposed that clumpy gas structures in cluster outskirts lead to an overestimate of the gas density, so that the outskirts entropy can be underestimated from X-ray observations. If high gas clumpiness is a dominant source of the flat entropy, a correlation between the outskirts entropy and the gas fraction is expected. However, in their simulations, gas clumpiness becomes dominant only beyond r_{200} . From *Suzaku* observations Simionescu et al. (2011) found an extremely-high gas fraction within the virial radius using their hydrostatic mass estimate for the Perseus cluster, and suggested that this is due to high gas clumpiness in the cluster outskirts. Here we argue that the cumulative gas fraction used by Simionescu et al. (2011) is not a good quantity to discuss the degree of gas clumpiness which is locally defined. Nevertheless, following Simionescu et al. (2011), we compare the outskirts entropy with the cumulative gas fractions within the virial radii, in the middle panel of Figure 3. Based on Simionescu et al. (2011), it is expected that the gas fraction is anti-correlated with the outskirts entropy. We find no clear correlation between K_{out} and $f_{\text{gas, vir}} \equiv f_{\text{gas}}(< r_{\text{vir}})$ for our three high-mass clusters. Since there is a possibility that the scatter in $K_{\text{out}} - f_{\text{gas, vir}}$ plane is caused by the mass dependence on the entropy (left panel), we show in the right panel a scaled version of the entropy normalized using the scaling relation. This shows that the scaled entropy does not correlate with the gas fraction, indicating that one cannot attribute the high gas fraction and low gas entropy to the gas clumping.

3.4. Universal Entropy Profile

Walker et al. (2012a) and Sato et al. (2012) showed that the entropy profiles for relaxed clusters have a universal form in the radial range from $\sim 0.1r_{200}$ to $\sim r_{200}$. In their analyses, they first normalize entropy profiles to unity at a certain pivot point (e.g., $0.3r_{200}$) and scale the cluster aperture radii by r_{200} which is determined according to the mass-temperature relation. Subsequently, fitting is performed to obtain the best-fit universal function. However, such scaling operations make it difficult to correctly propagate errors in the normalizations. Since we use the weak-lensing mass M_{Δ} and the aperture radius r_{Δ} for the normalizations, their errors should be explicitly taken into account.

To properly account for the errors in the weak-lensing and X-ray observables, we avoid two-steps procedures of Walker et al. (2012a) and Sato et al. (2012), and perform a simultaneous ensemble fit of the observed entropy profiles as a function of cluster radius and weak-lensing mass. The log-likelihood function is defined by

$$-2\ln\mathcal{L} = \sum_{i,j} \ln(\delta_{\ln K, ij}^2 + \delta_{\ln f, ij}^2 + \sigma_{\ln K}^2) + \frac{(\ln(K_i(r_j)) - \ln(f_K(M_i, r_j)))^2}{\delta_{\ln K, ij}^2 + \delta_{\ln f, ij}^2 + \sigma_{\ln K}^2}, \quad (2)$$

where i and j denote the i -th cluster and j -th radial bin,

respectively. $\delta_{\ln K}$ is the fractional error of the entropy, $\delta_{\ln f}$ is the fractional error in the function f_K , through its dependence on the total mass M_{Δ} and the aperture radius r_{Δ} from weak-lensing, and $\sigma_{\ln K}$ denotes intrinsic scatter of the entropy in the mass scaling relation. Here we have introduced the function f_K , which takes into account the flattening of the outskirts entropy profile, given by

$$f_K(M_{\Delta}, \tilde{r}) = K_0 E(z)^{-4/3} \left(\frac{M_{\Delta} E(z)}{10^{14} h_{70}^{-1} M_{\odot}} \right)^a \times (\tilde{r}/\tilde{r}_0)^{\alpha} (1 + (\tilde{r}/\tilde{r}_0)^{\beta})^{-\alpha/\beta}, \quad (3)$$

where K_0 is the normalization factor, $\tilde{r} = r/r_{\Delta}$ is the aperture radius in units of r_{Δ} , a is the mass slope, and r_0 denotes a characteristic scale radius at which the logarithmic entropy gradient changes. The asymptotic behavior is $K(r) \propto r^{\alpha}$ and $K(r) \propto \text{constant}$ for $r \ll r_0$ and $r \gg r_0$, respectively. All errors in M_{Δ} , r_{Δ} and K are considered.

We perform fitting of two X-ray datasets. The first dataset is composed only of the *Suzaku* data for the four clusters. The second one includes the *XMM-Newton* and *Chandra* as well as *Suzaku* data. We restrict our X-ray data to $r > 0.1r_{200}$ to excise the core regions. The fitting is performed both with and without intrinsic scatter.

Since the *Suzaku* data alone cannot constrain the β parameter, we fix $\beta = 4$ without intrinsic scatter. The resulting Bayesian estimates of the model parameters are listed in Table 2. The results do not change significantly when we change β by ± 2 . The inner slope of the entropy profile, $\alpha = 1.18_{-0.44}^{+0.93}$, agrees with the power-law slope ($K \propto r^{1.1}$) of the accretion shock heating model (Tozzi & Norman 2001).

Next, we fit the full *Suzaku*, *XMM-Newton* and *Chandra* data with and without intrinsic scatter. The constraint on the inner slope, $\alpha = 1.11_{-0.13}^{+0.17}$, is significantly improved. The best-fit entropy function, which was obtained without intrinsic scatter taken into account, gives an excellent description of the scaled entropy profiles of the four clusters (Figure 4). The mass dependence of the entropy is consistent with the self-similar model ($a = 2/3$). The inner radial slope α is in a remarkably good agreement with the shock heating model (Tozzi & Norman 2001) and with results from previous X-ray studies (e.g. Ponman et al. 2003). The flattening of the entropy profile occurs at $r \sim 0.5r_{200} \sim r_{1000}$, where the averaged hydrostatic to weak-lensing mass ratio is less than unity (Section 3.1).

We note that the four clusters studied here span a range of halo mass, concentration, X-ray luminosity and redshift, but exhibit a remarkable self-similarity in the scaled entropy profiles over the entire cluster ($> 0.1r_{200}$). In other words, not only the $r^{1.1}$ -law's entropy profile but also the outskirts flattening entropy depends on cluster M_{200} masses and r_{200} radius. The results indicate that the thermalization process in the ICM outside X-ray cores could be governed by the gravity of the cluster. The efficiency of gravitational heating from outside the core to $0.5r_{200}$ follows the accretion shock heating model (Tozzi & Norman 2001), whereas the efficiency at $r \gtrsim 0.5r_{200}$ is lower than the model prediction. The universality, inde-

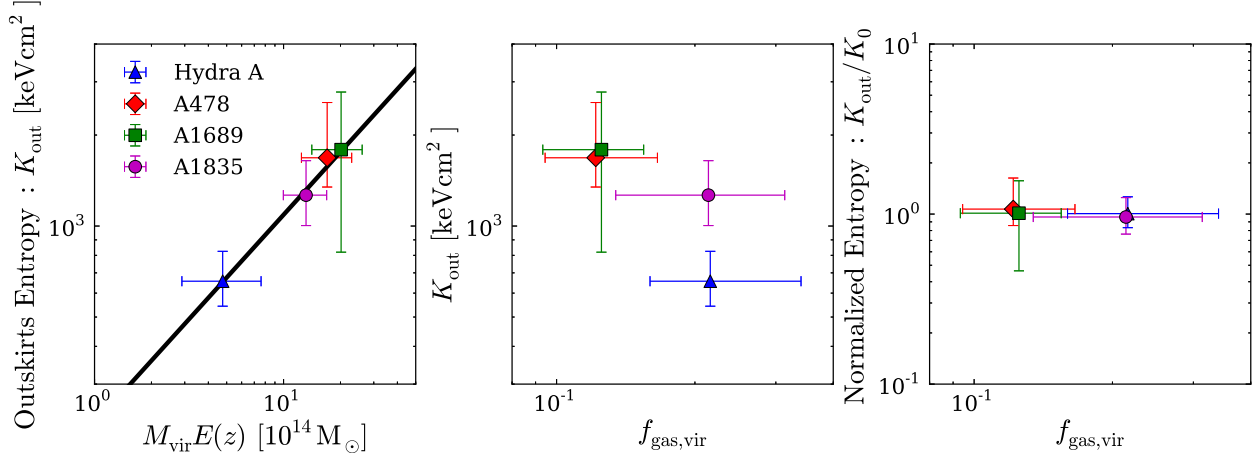


Fig. 3. Left: outskirts entropy (K_{out}) versus virial mass (M_{vir}) from lensing. The correction factor $E(z) = H(z)/H_0$ accounts for the redshift evolution. Outskirts entropy is highly correlated with the virial mass. Middle: outskirts entropy versus gas fraction within the virial radius ($f_{\text{gas,vir}}$). Right: outskirts entropy normalized by the $K_{\text{out}} - M_{\text{vir}}$ scaling relation ($K_0 = K(M_{\text{vir}})$) versus gas fraction. No significant correlation between the outskirts entropy and gas fractions is found.

pendent of cluster properties, indicates that the thermalization mechanism at work in the ICM could be a common physical process to all clusters, perhaps controlled by the growth of large scale structure surrounding the cluster, although the heating efficiency in the outskirts may need to be modified from the standard shock-heating mechanism (Tozzi & Norman 2001).

We also fit our data with an alternative functional form of $K \propto \tilde{r}^A \exp(B(1 - \tilde{r}))$ proposed by Lapi et al. (2010) and Cavaliere et al. (2011), by including our normalization parameter and using $\tilde{r} = r/r_{\text{vir}}$. We find this model also gives a good fit to the data. To statistically distinguish these two models, we need a larger sample of cluster observations with a wide radial coverage beyond the virial radius.

3.5. Universal Pressure Profile

It was shown by Planck Collaboration et al. (2013c) that the stacked pressure profile $P_e = n_e k_B T$ constructed from *Planck* SZ observations of 62 clusters is well described by a generalized NFW pressure profile (Nagai et al. 2007a) out to $3 \times r_{500}$. It is of great importance to compare our independent *Suzaku* X-ray pressure measurements to the *Planck* SZ observations (Walker et al. 2012b).

Here, we derive the average electron pressure profile scaled with the weak-lensing mass M_{Δ} following the same procedure described in Section 3.4. We consider the universal pressure function (Nagai et al. 2007a; Planck Collaboration et al. 2013c) of the following form, by simultaneously taking into account the scaling relation between the electron pressure and total mass M_{Δ} :

$$f_P(M_{\Delta}, \tilde{r}) = P_0 E(z)^2 \left(\frac{M_{\Delta} E(z)}{10^{14} h_{70}^{-1} M_{\odot}} \right)^b \times (\tilde{r}/\tilde{r}_0)^{-\gamma} (1 + (\tilde{r}/\tilde{r}_0)^{\beta})^{(\gamma-\delta)/\beta}, \quad (4)$$

where P_0 is the normalization factor, $\tilde{r} = r/r_{\Delta}$ is the aperture radius in units of r_{Δ} , and the mass slope b accounts for the dependence of the pressure normalization on the

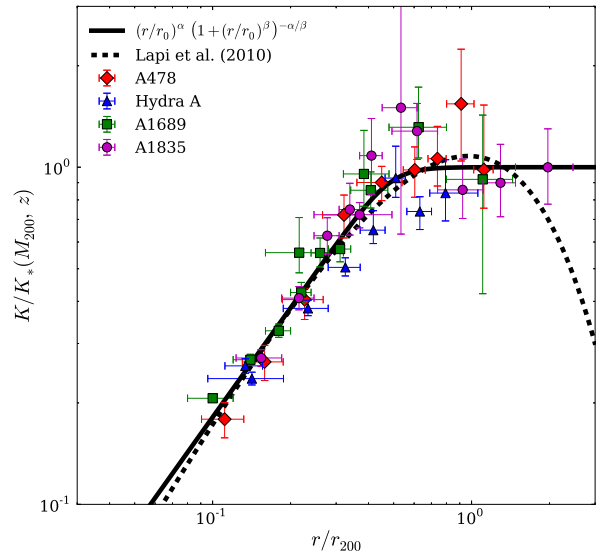


Fig. 4. Normalized entropy profile as a function of the radius scaled by r_{200} . Red diamonds, blue triangle, green squares and magenta circles denote the normalized entropy for A478, Hydra A, A1689, and A1835, respectively. The normalization is $K_*(M_{200}, z) = K_0 E(z)^{-4/3} (M_{200} E(z)/10^{14} h_{70}^{-1} M_{\odot})^a$, where $K_0 = 359.61$ [keV cm²] and $a = 0.63$. The black solid curve represents the best-fit universal entropy profile. The entropy profile at $r \lesssim 0.5 r_{200}$ follows $r^{1.1}$ as predicted by the standard model (Tozzi & Norman 2001) and becomes flat at $r \gtrsim 0.5 r_{200}$. The black-dashed curve shows the best-fit profile for the (Lapi et al. 2010) model.

Table 2. Best-fit parameters for the entropy profile. The results of the full *Suzaku*+*XMM-Newton*+*Chandra* data is referred to as “Full”.

Dataset	Δ	K_0 [keV cm ²]	a	α	β	r_0 [r_Δ]	$\sigma_{\ln K}$
<i>Suzaku</i>	200	$283.52^{+102.98}_{-80.71}$	$0.71^{+0.14}_{-0.11}$	$1.18^{+0.93}_{-0.44}$	4 (fixed)	$0.41^{+0.25}_{-0.16}$	—
Full	200	$359.61^{+92.00}_{-75.47}$	$0.63^{+0.09}_{-0.08}$	$1.11^{+0.17}_{-0.13}$	$5.97^{+2.49}_{-2.87}$	$0.48^{+0.10}_{-0.08}$	—
Full	200	$380.49^{+81.79}_{-71.61}$	$0.62^{+0.08}_{-0.07}$	$1.10^{+0.15}_{-0.13}$	5.97 (fixed)	$0.49^{+0.10}_{-0.07}$	< 0.06

halo mass M_Δ determined from the lensing analysis. The asymptotic entropy slopes are $P \propto r^{-\gamma}$ and $r^{-\delta}$ for $r \ll r_0$ and $r \gg r_0$, respectively. The inverse of the scale radius, $\tilde{r}_0^{-1} = r_\Delta/r_0$, is equivalent to the concentration parameter, c_Δ , in the definition of Planck Collaboration et al. (2013c).

First, we fit our pressure profiles at the reference overdensity $\Delta = 500$ to make a fair comparison with Planck Collaboration et al. (2013c). We fix r_0 and β by the *Planck* results ($c_{500} = \tilde{r}_0^{-1} = 1.81$ and $\beta = 1.33$), because it is difficult to constrain them from our data. The best-fit parameters are listed in Table 3. The normalized pressure profiles derived from the full *Suzaku*, *XMM-Newton* and *Chandra* dataset are displayed in Figure 5. The logarithmic gradient of the pressure profile progressively steepens from -1 to -4 .

For comparison, we calculate the normalized *Planck* pressure profiles using the equations (7), (10) and (11) of Planck Collaboration et al. (2013c). We use the best-fit parameters of the stacked pressure profile and determine the normalization by two approaches, namely using our weak-lensing or X-ray hydrostatic mass estimates, instead of their original mass estimates using the $Y_X = M_{\text{gas}} T_X$ mass proxy. Figure 5 shows that the *Planck* average pressure profiles agree with the *Suzaku* results. The outer slope δ is in excellent agreement with the average slope of the *Planck* SZ pressure profile ($\delta = 4.1$). Although our sample size is much smaller than that of the *Planck* sample, our results show good consistency between the observationally independent X-ray and SZ profiles of individual clusters (Walker et al. 2012b; Mochizuki et al. 2014).

Next, we fix $r_0 = 0.48r_{200}$ and $\beta = 5.97$ using the best-fit entropy profile (Section 3.4). Now we derive scaled profiles at a density contrast of $\Delta = 200$. The best-fit pressure profile, converted to r_{500} units, is shown in Figure 5. The resulting pressure profile is compatible with our and the average *Planck* pressure profiles. We also measure intrinsic scatter with $b = 2/3$ fixed (Table 3). Some parameters, including b , γ , and δ , are slightly changed depending on the choice of β and r_0 . A more definitive determination of these parameters requires a further systematic study.

3.6. Joint Fit with the Number Density and Temperature Profiles

In Sections 3.4 and 3.5, we have shown that the scaled entropy and pressure profiles of the four clusters are well fitted with respective universal functions, by taking into account the uncertainties in the weak-lensing mass and X-ray measurements.

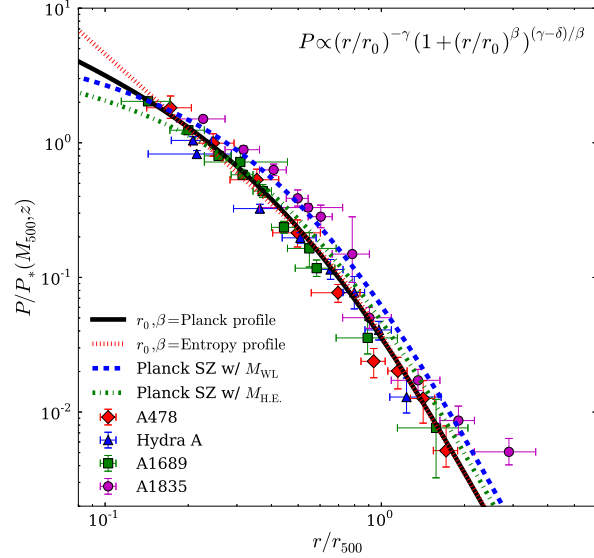


Fig. 5. Normalized pressure profile as a function of cluster radius scaled by r_{500} . Red diamonds, blue triangle, green squares and magenta circles represent the normalized pressure for A478, Hydra A, A1689, and A1835, respectively. The normalization is $P_*(M_{500}, z) = P_0 E(z)^{1/2} (M_{500} E(z)/10^{14} h_{70}^{-1} M_\odot)^b$. The black-solid and red-dotted lines are the best-fit profiles using r_0 and β from the *Planck* results (Planck Collaboration et al. 2013c) and our best-fit entropy profile, respectively. The blue-dashed and green-dotted-dashed lines are the average SZ pressure profiles (Planck Collaboration et al. 2013c), obtained using the weak-lensing and hydrostatic masses, respectively.

Here we simultaneously fit the gas density and temperature profiles to our X-ray observations for determining the respective universal functions. From equations (3) and (4), we obtain the following expressions for the gas number density and temperature:

$$f_n = n_0 E(z)^2 \left(\frac{M_\Delta E(z)}{10^{14} h_{70}^{-1} M_\odot} \right)^{\frac{3}{5}(b-a)} \times (\tilde{r}/\tilde{r}_0)^{-\frac{3}{5}(\alpha+\gamma)} (1 + (\tilde{r}/\tilde{r}_0)^\beta)^{-\frac{3}{5}(\delta-\gamma-\alpha)/\beta}, \quad (5)$$

$$f_T = T_0 \left(\frac{M_\Delta E(z)}{10^{14} h_{70}^{-1} M_\odot} \right)^{\frac{3}{5}a + \frac{2}{5}b} \times (\tilde{r}/\tilde{r}_0)^{\frac{3}{5}\alpha - \frac{2}{5}\gamma} (1 + (\tilde{r}/\tilde{r}_0)^\beta)^{-(\frac{2}{5}\delta - \frac{2}{5}\gamma + \frac{3}{5}\alpha)/\beta}, \quad (6)$$

Table 3. Best-fit parameters for the pressure profile. “Full” refers to the full *Suzaku*+*XMM-Newton*+*Chandra* dataset.

Dataset	Δ	$\log_{10}(P_0)$ [log(keV cm ⁻³)]	b	β	γ	δ	r_0 [r_Δ]	$\sigma_{\ln P}$
<i>Suzaku</i>	500	$-2.41^{+0.17}_{-0.17}$	$0.43^{+0.10}_{-0.10}$	1.33 (fixed)	$1.08^{+0.25}_{-0.25}$	$3.41^{+0.42}_{-0.38}$	1/1.81 (fixed)	—
Full	500	$-2.00^{+0.15}_{-0.14}$	$0.08^{+0.07}_{-0.05}$	1.33 (fixed)	$0.81^{+0.22}_{-0.21}$	$4.07^{+0.36}_{-0.35}$	1/1.81 (fixed)	—
Full	500	$-2.35^{+0.2}_{-0.21}$	$0.15^{+0.10}_{-0.08}$	1.33 (fixed)	$1.24^{+0.38}_{-0.38}$	$4.07^{+0.36}_{-0.35}$	1/1.81 (fixed)	$0.24^{+0.10}_{-0.06}$
Full	200	$-3.14^{+0.16}_{-0.16}$	$0.32^{+0.14}_{-0.14}$	5.97 (fixed)	$1.84^{+0.17}_{-0.15}$	$3.45^{+0.43}_{-0.36}$	0.48 (fixed)	—
Full	200	$-2.85^{+0.38}_{-0.36}$	2/3 (fixed)	$5.54^{+2.81}_{-2.84}$	$1.26^{+0.44}_{-0.79}$	$2.67^{+0.30}_{-0.21}$	$0.24^{+0.11}_{-0.07}$	$0.28^{+0.10}_{-0.09}$

where M_Δ is the total cluster mass from lensing measurements, n_0 and T_0 are the normalization factors for the gas density and temperature profiles, respectively. Here we have assumed that the gas density and temperature profiles have the same scale radius r_0 and β .

The joint likelihood for the number density and the temperature profiles is given by

$$\begin{aligned}
 -2 \ln \mathcal{L} &= \sum_{i,j} \ln(\det(\mathbf{C}_{ij})) + \mathbf{v}_{ij}^T \mathbf{C}_{ij}^{-1} \mathbf{v}_{ij}, \\
 \mathbf{v} &= \begin{pmatrix} \ln(n(\tilde{r})) - \ln(f_n(M_\Delta, \tilde{r})) \\ \ln(T(\tilde{r})) - \ln(f_T(M_\Delta, \tilde{r})) \end{pmatrix}, \\
 \mathbf{C} &= \mathbf{C}_{\text{stat}} + \mathbf{C}_{\text{int}} \\
 \mathbf{C}_{\text{stat}} &= \begin{pmatrix} \delta_{\ln n}^2 + \delta_{\ln f_n}^2 & \delta_{\ln f_n, \ln f_T} \\ \delta_{\ln f_n, \ln f_T} & \delta_{\ln T}^2 + \delta_{\ln f_T}^2 \end{pmatrix}, \\
 \mathbf{C}_{\text{int}} &= \begin{pmatrix} \sigma_{\ln n}^2 & \rho \sigma_{\ln n} \sigma_{\ln T} \\ \rho \sigma_{\ln n} \sigma_{\ln T} & \sigma_{\ln T}^2 \end{pmatrix}.
 \end{aligned} \tag{7}$$

Here, i and j denote the i -th cluster and j -th radial bins, respectively. \mathbf{C}_{stat} is the error covariance matrix for the data vector \mathbf{v} , $\delta_{\ln n}$ and $\delta_{\ln T}$ are the fractional errors of the gas density and temperature, $\sigma_{\ln f_n}$ and $\sigma_{\ln f_T}$ are the fractional errors in the functions f_n and f_T (see equations (5) and (6)) through their weak-lensing mass dependence. We assume that the error correlation between the number density and the temperature is negligible. Note that the off-diagonal elements in the covariance matrix cannot be ignored because both the gas density and temperature depend on the weak-lensing mass. The intrinsic covariance \mathbf{C}_{int} consists of intrinsic scatter of the number density $\sigma_{\ln n}$ and the temperature $\sigma_{\ln T}$. By definition the correlation coefficient ρ is in the range $-1 \leq \rho \leq 1$.

Since the number density and temperature profiles are equivalent to the entropy and pressure profiles which have been investigated in Sections 3.4 and 3.5, we shall focus on the results of the intrinsic covariance based on the self-similar solution ($a = b = 2/3$). For this, we use the full *Suzaku*, *XMM-Newton* and *Chandra* dataset. The best-fit profiles of gas density and temperature are shown in the top panel of Figure 6. The pressure and entropy profiles corresponding to the best-fit parameters (Table 4) are shown in the bottom panel of Figure 6. The normalization factors for the gas density, temperature, pressure, and entropy are $n_* = n_0 E(z)^2 (M_{200} E(z))^{3(b-a)/5}$, $T_* = T_0 (M_{200} E(z))^{3b/5+2a/5}$, $P_* = n_0 T_0 E(z)^2 (M_{200} E(z))^b$ and $K_* = T_0 n_0^{-2/3} E(z)^{-4/3} (M_{200} E(z))^a$, respectively.

The best-fit density profile describes well the observations as shown in the top-left panel of Figure 6. The residual deviation $\Delta_{\text{dev}} = n/f_n - 1$ from the best-fit profile is shown in the lower subpanel. Compared to A478 and A1689, the deviations for Hydra A and A1835, corresponding to the clusters with high gas fractions (Figure 2), are high but constant with radius r/r_{200} , showing that the observed scaled density profiles follow the universal trend within intrinsic scatter. The logarithmic gradient of the gas density slightly changes from $d \ln n_e / d \ln r = -3(\alpha + \gamma)/5 \sim -1.9$ at $r \ll r_0$ to $-3\delta/5 \sim -1.6$ at $r \gg r_0$. The gas density slope outside the X-ray cores ($r > 0.1 r_{200}$) is thus shallower than the outer asymptotic slope of the NFW density profile (-3). Similar results were reported in previous studies of *Chandra* and *XMM-Newton* observations (e.g. Vikhlinin et al. 2006; Zhang et al. 2008). A possible interpretation of the apparent shallow outer slope is that the degree of gas clumpiness is increased in the cluster outskirts (Nagai & Lau 2011).

The X-ray temperature profiles are nearly constant at $0.1 r_{200} \lesssim r \lesssim 0.5 r_{200}$, which is consistent with previous studies (e.g. Vikhlinin et al. 2006; Zhang et al. 2008). The logarithmic slope of the temperature drastically changes at $\sim 0.5 r_{200}$ from $3\alpha/5 - 2\gamma/5 \sim 0$ to $-2\delta/5 \sim -1.1$. The deviation $\Delta_{\text{dev}} = T/f_T - 1$ is constant with radius and close to zero, showing high similarity of the temperature profiles over a wide radial range.

For the gas pressure, the logarithmic gradient steepens from $d \ln P / d \ln r = -\gamma \sim -1.8$ to $-\delta \sim -2.7$ over the full radial range (see Section 3.5 for the case of $\Delta = 500$). The deviations $P/f_P - 1$ of Hydra A and A1835 are higher than those of A1689 and A478, which reflects the large deviations in the gas density.

The entropy profile increases with radius as $\propto r^{1.16}$ at $r \lesssim 0.5 r_{200}$, and then flattens at radii greater than $\sim 0.5 r_{200}$. The inner slope is consistent with the gravitational shock heating model ($\propto r^{1.1}$; Tozzi & Norman 2001). Our results show that the entropy flattening in the outskirts is caused not by the shallow outer density slope but by the steep temperature drop. We find the density slope changes with radius only by $\sim +0.3$, corresponding to a slope change of ~ -0.2 for the entropy, $K \propto n^{-2/3}$. On the other hand, the steepening of the temperature slope by ~ -1.1 significantly affects the entropy slope because $K \propto T$.

Including the intrinsic covariance matrix in our analysis, we can constrain the intrinsic scatter between the X-ray

observables and weak-lensing masses. We find the intrinsic scatter of the gas density $\sigma_{\ln n}$ is greater than that of the temperature $\sigma_{\ln T}$ for our sample of the clusters. This is qualitatively consistent with the trends in the deviation profiles shown in Figure 6.

From Bayesian inference, we obtain a 1σ lower limit on the correlation coefficient, $\rho > 0.47$. On the other hand, we find a maximum-likelihood estimate of $\rho = 0.96$, which is high and close to the upper bound ($\rho = 1$) of the parameter range. We thus computed the probability $\mathcal{P}(\geq |\rho|)$ that the correlation coefficient of two random variables for a sample size of 4 is greater than 0.96, finding $\mathcal{P}(\geq |\rho|) = 0.04$, which is very small and rules out the possibility that the high correlation coefficient is randomly generated.

Since the intrinsic scatter of the quantity $X = Tn^p$ is expressed as $\sigma_{\ln X}^2 = \sigma_{\ln T}^2 + p^2 \sigma_{\ln n}^2 + 2p\rho\sigma_{\ln n}\sigma_{\ln T}$, the observed positive coefficient indicates that the third terms for the entropy ($p = -2/3$) and pressure ($p = 1$) are negative and positive, respectively. Thus, the intrinsic scatter of the entropy is smaller than that of the pressure, which is consistent with the results from individual analyses of the pressure and entropy (Sections 3.4 and 3.5). The positive correlation between the gas density and temperature can also be seen in their deviation profiles in Figure 6. Due to this positive correlation, the deviation amplitude for the pressure is larger than that for the entropy. Similarly, a joint X-ray and weak-lensing analysis of Okabe et al. (2010b) derived bivariate M - T and M - M_{gas} scaling relations for 12 clusters at $\Delta = 500$, finding that the intrinsic scatter between the gas mass and the temperature is positively correlated.

Theoretical predictions for the intrinsic correlation between the gas mass and pressure are rather controversial. Using an adaptive-mesh refinement code, Kravtsov et al. (2006) found from their simulations that the gas-temperature deviations from the M - T relation are anti-correlated with the gas-mass deviations from the M - M_{gas} relation. On the other hand, Stanek et al. (2010) showed that the temperature and gas-mass deviations are positively correlated with each other. Therefore, a larger sample is required to constrain the intrinsic correlations between cluster properties, and it will allow us to investigate the functional form of the radial profile with the lowest scatter and optimal mass proxies based on the principal component analysis (Okabe et al. 2010b).

Now we examine the validity of the hydrostatic-equilibrium assumption:

$$\frac{1}{\rho_g} \frac{dP_g}{dr} = -\frac{GM}{r^2}, \quad (8)$$

where ρ_g and P_g are the gas mass density and thermal pressure, respectively. Since $\rho_g \propto n_e$ and $P_g \propto P_e$, the best-fit parameters (Table 4) in equations (4) and (5) allow us to determine the radius beyond which the enclosed hydrostatic mass unphysically decreases (i.e., $dM/dr < 0$). We find that the breakdown of the assumption occurs at $r \sim 0.84r_{200} \sim 1.3r_{500}$, which is consistent with previous studies (e.g. Mochizuki et al. 2014; Kawaharada et al. 2010; Ichikawa et al. 2013). The breakdown of the hy-

drostatic assumption underestimates hydrostatic mass estimates at $r \gtrsim 1.3r_{500}$. Indeed, Figure 1 shows that the hydrostatic masses are on average much lower than the weak-lensing masses at $r > r_{500}$.

The methodology we have applied here, which simultaneously fits X-ray observable profiles taking into account multivariate scaling relations, stems from our earlier work on the multivariate scaling relations (Okabe et al. 2010b). In the traditional method, one obtains scaling relations between the total mass and X-ray observables at a given reference overdensity (e.g., $\Delta = 200$ or 500). Furthermore, we have also established the average scaled radial profiles and intrinsic scatters for X-ray observables. In contrast to the traditional method, this new method enables us to simultaneously constrain the shape of the radial profile, normalization, and its intrinsic scatter, where the normalization of the profile corresponds to the mass-observable scaling relation. Importantly, this method does not require an iterative procedure to reconstruct mass-observable scaling relations (Vikhlinin et al. 2009a) because the scaling parameters at specific overdensities are determined by lensing and hence independent of X-ray observables.

We note that this method is complementary to stacking approaches (Planck Collaboration et al. 2013c; Okabe et al. 2013; Umetsu et al. 2014), which allow us to derive ensemble-averaged cluster profiles in a model-independent way. This new method to measure the characteristic shapes and normalizations of profiles will provide us a powerful means to establish the mass proxy for cluster cosmology studies, especially for the forthcoming large-scale X-ray surveys (e.g. *eROSITA*).

4. Summary

We have performed a joint X-ray and weak-lensing analysis of a sample of four relaxed clusters (Hydra A, A478, A1689, and A1835), which had been deeply observed to date by both *Suzaku* and Subaru out to virial radii. We have shown that the X-ray hydrostatic mass estimates are systematically underestimated, where the average hydrostatic-to-lensing mass ratio decreases from $\sim 70\%$ at r_{500} to $\sim 30\%$ at r_{vir} . This radial dependence is detected at the 3σ significance level. The average gas mass fraction from weak-lensing mass estimates increases with radius, and agrees with the cosmic baryon fraction within the virial radius. The outskirts entropy is shown to be tightly correlated with the total cluster mass from lensing, but not with the gas mass fraction within the virial radii.

We have developed a new advanced method for determining normalized cluster radial profiles for multiple X-ray observables by simultaneously taking into account both their radial dependence and multivariate scaling relations with weak-lensing masses. This method stems from the techniques for determining the multivariate scaling relations (Okabe et al. 2010b) and is complementary to stacking approaches. In the paper, we first used this method to individually reconstruct each universal X-ray observable function (Sections 3.4 and 3.5). We then ap-

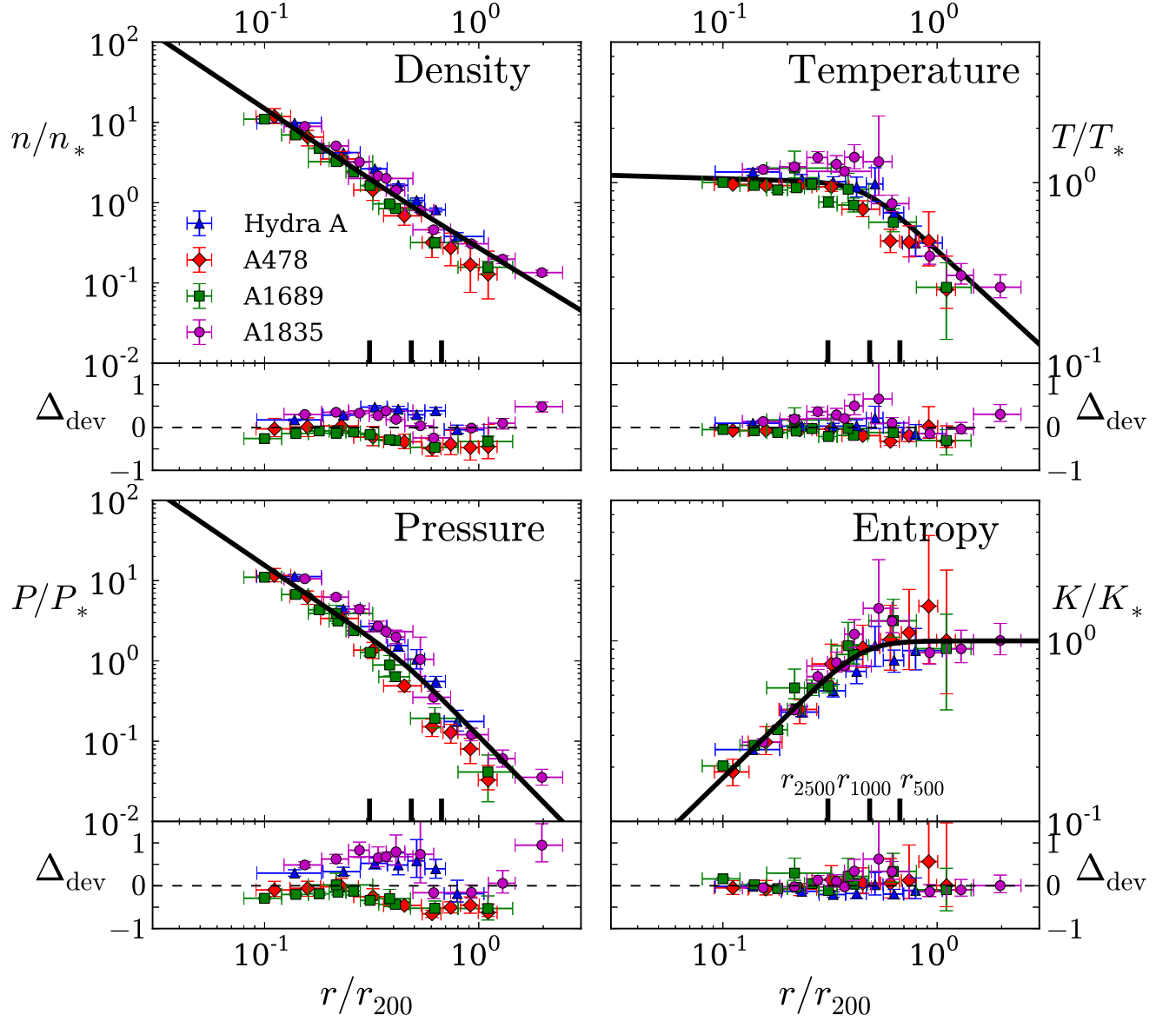


Fig. 6. Normalized radial profiles of gas number density (top-left), temperature (top-right), pressure (bottom-left) and entropy (bottom-right), obtained from joint analysis of the observed gas density and temperature profiles. Red diamonds, blue triangle, green squares and magenta circles represent the normalized data for A478, Hydra A, A1689, and A1835, respectively. The black-solid curves show the best-fit models. The lower subpanels show the deviations from the respective best-fit profiles. The overall amplitude of deviations is different from cluster to cluster, reflecting the intrinsic scatter between the X-ray observables and weak-lensing mass. The deviations are almost constant with radius, indicating that the scaled X-ray profiles are fairly universal. The black vertical bars denote r_{2500} , r_{1000} , and r_{500} , from left to right.

Table 4. Best-fit parameters for the universal entropy and pressure function (equations (3) and (4)), obtained from a simultaneous fit to the observed electron number density, X-ray temperature, and weak-lensing masses.

$\log_{10}(n_0)$ $\log_{10}(1\text{cm}^{-3})$	T_0 [keV]	a	b	α	β
$-3.60^{+0.15}_{-0.14}$	$1.27^{+0.24}_{-0.19}$	2/3 (fixed)	2/3 (fixed)	$1.16^{+0.17}_{-0.12}$	$5.52^{+2.87}_{-2.64}$
γ	δ	r_0 [r_{200}]	$\sigma_{\ln n}$	$\sigma_{\ln T}$	ρ
$1.82^{+0.28}_{-0.30}$	$2.72^{+0.34}_{-0.35}$	$0.45^{+0.08}_{-0.07}$	$0.22^{+0.05}_{-0.04}$	$0.07^{+0.06}_{-0.04}$	> 0.49

plied it to simultaneously determine two X-ray observable functions by taking into account their intrinsic covariance (Section 3.6). A combination of complementary data sets of the weak-lensing masses and radii and X-ray observables is essential to this method.

We find the gas entropy, pressure, and density profiles are all remarkably self-similar when scaled with the weak-lensing M_{200} mass and r_{200} radius. The entropy monotonically increases out to $\sim 0.5r_{200} \sim r_{1000}$ following the accretion shock heating model $K(r) \propto r^{1.1}$ (Tozzi & Norman 2001), and flattens at $\gtrsim 0.5r_{200}$. The logarithmic gradient of the gas density becomes slightly shallower at $r \sim 0.5r_{200}$. A possible interpretation for this is that the degree of gas clumpiness is increased in the outskirts. The temperature profile is constant at $0.1r_{200} < r < \lesssim 0.5r_{200}$, and sharply drops off outside $\sim 0.5r_{200}$. The bivariate scaling functions of the gas density and temperature reveal that the flatness of the outskirts entropy profile is caused by the steepening of the temperature, rather than the flattening of the gas density. Thus, gas clumpiness alone cannot be responsible for all of the flatness of the outskirts entropy. The pressure profile exhibits a steep outer slope, in good agreement with the averaged *Planck* Sunyaev-Zel'dovich pressure profile. The assumption of hydrostatic equilibrium breaks down beyond $\sim 0.84r_{200} \sim 1.3r_{500}$.

Our cluster sample may not be representative of a homogeneous class of actual clusters because the clusters were selected solely by the current availability of both *Suzaku* and Subaru observations. The sample clusters span a range of halo mass, concentration, X-ray luminosity and redshift. Nevertheless, we find the universality of the scaled entropy profiles. This indicates that the thermalization mechanism in the ICM over the entire region ($> 0.1r_{200}$) is controlled by gravitation in a common way for all clusters. The entropy flattening in cluster outskirts appears to be a common phenomena, not limited to a special class of clusters. This demonstrates that the heating efficiency in the outskirts needs to be modified from the standard $r^{1.1}$ law. Since the current sample is small and limited by the availability of data, a further systematic multi-wavelength study of cluster outskirts is vitally important to understand the physical state of the ICM.

Acknowledgments

This work was supported by World Premier International Research Center Initiative (WPI Initiative),

MEXT, Japan. N. Okabe (26800097), M. Takizawa (26400218), and K. Sato (25800112) are supported by a Grant-in-Aid from the Ministry of Education, Culture, Sports, Science, and Technology of Japan. K. Umetsu acknowledges partial support from the National Science Council of Taiwan (grant NSC100-2112-M-001-008-MY3). Y. -Y. Zhang acknowledges support by the German BMWi through the Verbundforschung under grant 50 OR 1304.

References

- Bartelmann, M., & Schneider, P. 2001, *Phys. Rep.*, 340, 291
- Bautz, M. W., Miller, E. D., Sanders, J. S., et al. 2009, *PASJ*, 61, 1117
- Cavagnolo, K. W., Donahue, M., Voit, G. M., & Sun, M. 2009, *ApJS*, 182, 12
- Cavaliere, A., Lapi, A., & Fusco-Femiano, R. 2011, *ApJ*, 742, 19
- David, L. P., Nulsen, P. E. J., McNamara, B. R., et al. 2001, *ApJ*, 557, 546
- Fujita, Y., Ohira, Y., & Yamazaki, R. 2013, *ApJ*, 767, L4
- Fujita, Y., Tawa, N., Hayashida, K., et al. 2008, *PASJ*, 60, 343
- Hinshaw, G., Larson, D., Komatsu, E., et al. 2013, *ApJS*, 208, 19
- Hoshino, A., Henry, J. P., Sato, K., et al. 2010, *PASJ*, 62, 371
- Ichikawa, K., Matsushita, K., Okabe, N., et al. 2013, *ApJ*, 766, 90
- Kawaharada, M., Okabe, N., Umetsu, K., et al. 2010, *ApJ*, 714, 423
- Kravtsov, A. V., Vikhlinin, A., & Nagai, D. 2006, *ApJ*, 650, 128
- Lapi, A., Fusco-Femiano, R., & Cavaliere, A. 2010, *A&A*, 516, A34
- Lau, E. T., Kravtsov, A. V., & Nagai, D. 2009, *ApJ*, 705, 1129
- Lau, E. T., Nagai, D., & Nelson, K. 2013, *ApJ*, 777, 151
- Mahdavi, A., Hoekstra, H., Babul, A., et al. 2013, *ApJ*, 767, 116
- Meneghetti, M., Rasia, E., Vega, J., et al. 2014, *ArXiv e-prints*
- Mitsuda, K., Bautz, M., Inoue, H., et al. 2007, *PASJ*, 59, 1
- Miyazaki, S., Komiyama, Y., Sekiguchi, M., et al. 2002, *PASJ*, 54, 833

- Mochizuki, Y., , et al. 2014, *ApJ*, submitted
- Nagai, D., Kravtsov, A. V., & Vikhlinin, A. 2007a, *ApJ*, 668, 1
- Nagai, D., & Lau, E. T. 2011, *ApJ*, 731, L10
- Nagai, D., Vikhlinin, A., & Kravtsov, A. V. 2007b, *ApJ*, 655, 98
- Nakamura, T. T., & Suto, Y. 1997, *Progress of Theoretical Physics*, 97, 49
- Navarro, J. F., Frenk, C. S., & White, S. D. M. 1996, *ApJ*, 462, 563
- . 1997, *ApJ*, 490, 493
- Nelson, K., Lau, E. T., Nagai, D., Rudd, D. H., & Yu, L. 2014, *ApJ*, 782, 107
- Oguri, M., Bayliss, M. B., Dahle, H., et al. 2012, *MNRAS*, 420, 3213
- Oguri, M., & Keeton, C. R. 2004, *ApJ*, 610, 663
- Okabe, N., Smith, G. P., Umetsu, K., Takada, M., & Futamase, T. 2013, *ApJ*, 769, L35
- Okabe, N., Takada, M., Umetsu, K., Futamase, T., & Smith, G. P. 2010a, *PASJ*, 62, 811
- Okabe, N., Zhang, Y.-Y., Finoguenov, A., et al. 2010b, *ApJ*, 721, 875
- Okabe, N., Umetsu, K., Tamura, T., et al. 2014, *ArXiv e-prints*
- Piffaretti, R., Arnaud, M., Pratt, G. W., Pointecouteau, E., & Melin, J.-B. 2011, *A&A*, 534, A109
- Piffaretti, R., & Valdarnini, R. 2008, *A&A*, 491, 71
- Planck Collaboration, Ade, P. A. R., Aghanim, N., et al. 2013a, *ArXiv e-prints*
- . 2013b, *ArXiv e-prints*
- . 2013c, *A&A*, 550, A131
- Ponman, T. J., Sanderson, A. J. R., & Finoguenov, A. 2003, *MNRAS*, 343, 331
- Pratt, G. W., Arnaud, M., Piffaretti, R., et al. 2010, *A&A*, 511, A85
- Reiprich, T. H., Basu, K., Ettori, S., et al. 2013, *Space Sci. Rev.*, 177, 195
- Richard, J., Smith, G. P., Kneib, J.-P., et al. 2010, *MNRAS*, 404, 325
- Sanderson, A. J. R., Finoguenov, A., & Mohr, J. J. 2005, *ApJ*, 630, 191
- Sato, T., Sasaki, T., Matsushita, K., et al. 2012, *PASJ*, 64, 95
- Simionescu, A., Allen, S. W., Mantz, A., et al. 2011, *Science*, 331, 1576
- Stanek, R., Rasia, E., Evrard, A. E., Pearce, F., & Gazzola, L. 2010, *ApJ*, 715, 1508
- Tozzi, P., & Norman, C. 2001, *ApJ*, 546, 63
- Umetsu, K., & Broadhurst, T. 2008, *ApJ*, 684, 177
- Umetsu, K., Broadhurst, T., Zitrin, A., et al. 2011, *ApJ*, 738, 41
- Umetsu, K., Medezinski, E., Nonino, M., et al. 2014, *ArXiv e-prints*
- Vikhlinin, A., Kravtsov, A., Forman, W., et al. 2006, *ApJ*, 640, 691
- Vikhlinin, A., Burenin, R. A., Ebeling, H., et al. 2009a, *ApJ*, 692, 1033
- Vikhlinin, A., Kravtsov, A. V., Burenin, R. A., et al. 2009b, *ApJ*, 692, 1060
- Walker, S. A., Fabian, A. C., Sanders, J. S., & George, M. R. 2012a, *MNRAS*, 427, L45
- Walker, S. A., Fabian, A. C., Sanders, J. S., George, M. R., & Tawara, Y. 2012b, *MNRAS*, 422, 3503
- Walker, S. A., Fabian, A. C., Sanders, J. S., Simionescu, A., & Tawara, Y. 2013, *MNRAS*, 432, 554
- Zhang, Y.-Y., Finoguenov, A., Böhringer, H., et al. 2007, *A&A*, 467, 437
- . 2008, *A&A*, 482, 451
- Zhang, Y.-Y., Okabe, N., Finoguenov, A., et al. 2010, *ApJ*, 711, 1033